Thermally Induced Atomic Reconstruction of Twisted Transition Metal Dichalcogenide Layers into Fully Commensurate Structures

Ji-Hwan Baek[1], Hyoung Gyun Kim[1], Soo Yeon Lim[2], Seong Chul Hong[1], Yunyeong Chang[1], Huije Ryu[1], Yeonjoon Jung[1], Hajung Jang[2], Jungcheol Kim[2], Yichao Zhang[5] Kenji Watanabe[3], Takashi Taniguchi[4], Pinshane Y. Huang[5], Hyeonsik Cheong[2], Miyoung Kim[1], Gwan-Hyoung Lee[1]*

[1]Department of Material Science and Engineering, Seoul National University, Seoul 08826, Korea
[2]Department of Physics, Sogang University, Seoul 04107, Korea
[3]Research Center for Functional Materials, National Institute for Materials Science, 1-1 Namiki, Tsukuba 305-0044, Japan
[4]International Center for Materials Nanoarchitectonics, National Institute for Materials Science, 1-1 Namiki, Tsukuba 305-0044, Japan
[5]Department of Materials Science and Engineering, University of Illinois at Urbana-Champaign, IL 61820, USA
*Corresponding author. E-mail: *gwanlee@snu.ac.kr*

Abstract

Twist angle between two-dimensional (2D) layers is a critical parameter that determines their interfacial properties of van der Waals heterostructure, such as moiré excitons and interfacial ferroelectricity. To achieve better control over these properties for fundamental studies and various applications, there have been considerable efforts to manipulate the twist angle. Despite rigorous efforts to control the twist angle of stacked two-dimensional (2D) layers, there remains a challenge in perfectly aligning the crystalline orientation due to mechanical limitations and the inevitable formation of incommensurate regions. Here, we report a thermally activated atomic reconstruction of randomly stacked transition metal dichalcogenides (TMDs) multilayers into fully commensurate (FC) heterostructures with zero-twist-angle by encapsulation annealing, regardless of twist angles of as-stacked samples and large lattice mismatches. We also demonstrate the selective formation of R- and H-type FC phases with a seamless lateral junction using chemical-vapor-deposited TMDs. The resulting FC phases exhibit strong photoluminescence (PL) enhancement of the interlayer excitons even at room temperature due to their commensurate structure with aligned momentum coordinates. Our work not only shows a way to fabricate zero-twisted 2D bilayers with R and H-type configurations, but also provides a platform for studying their unexplored properties, such as interlayer excitons, interlayer valley, and interlayer ferroelectrics.

Introduction

Van der Waals (vdW) heterostructures of 2D layers have been widely studied owing to their unprecedented physical properties, such as superconductivity and Mott insulating phase in magic-angle graphene bilayer and moiré interlayer excitons and quantum-mechanically hybridized electronic states in twisted TMD bilayers[1-9]. Therefore, the twist angle of two stacked layers has been considered as a critical parameter to determine electronical and optical properties of the twisted vdW

heterostructures[10-13]. However, recent reports indicate that the twisted bilayers undergo unconventional atomic reconstruction to relieve strain[14-19], with stacked bilayers with large twist angles forming the moiré superlattice structures due to the high energy required for the atomic reconstruction[15,20], and nearly-zero-stacked bilayers transforming into periodic commensurate domains separated by incommensurate (IC) boundaries with renormalized electronic band structures[14,21]. Although zero-twisted bilayers are energetically stable in theory, the challenge lies in achieving perfect alignment of stacked 2D layers due to the inaccuracy of mechanical manipulators and inevitable formation of IC boundaries as a result of the spontaneous reconstruction.

Here, we present a method for achieving fully commensurate (FC) heterostructures with zero-twist angle by a thermally induced atomic reconstruction of twisted 2D layers using encapsulation annealing regardless of twist angles of the as-stacked and lattice mismatches, resulting in perfectly aligned crystalline orientations of H- or R-type over entire stacked area and opposite strains in adjacent layers. The FC heterostructure of two TMDs shows strong photoluminescence (PL) enhancement of interlayer excitons, reaching a thermal limit, due to aligned electronic band edges in momentum space. We also demonstrate selective formation of R- and H-type FC phases with seamless lateral junction by stacking 2D layers with parallel or anti-parallel alignment of two constituent TMD layers.

Encapsulation annealing of twisted TMD layers

In order to prevent decomposition of TMD layers and provide encapsulation-induced pressure during annealing[22-25], we fabricated twisted TMD hetero-bilayers encapsulated by graphene or hBN, as illustrated in Fig. 1a. The MX_2 (M = W, Mo and X = S, Se) was synthesized into triangular grains by chemical vapor deposition (CVD), which allows us to determine the stacking types of TMD bilayers by aligning two grains: R-stack for parallel alignment and H-stack for anti-parallel alignment. (See methods for synthesis of TMDs and Fig. S1-2 for alignment of stacked layers). Fig. 1b shows the optical microscopic image of R- and H-stacks of $WSe_2/MoSe_2$ by aligning triangular edges of TMD monolayers. As shown in high-angle annular dark-field scanning transmission electron microscopy (HAADF-STEM) image of Fig. 1c, the moiré superlattices were observed in the as-stacked H-$WSe_2/MoSe_2$ with a twist angle of 46.9˚ (measured using selected area electron diffraction (SAED) patterns). Note that we used graphene for encapsulation instead of hBN in order to obtain clear TEM images. However, after encapsulation annealing at 800˚C for 3 h, the twisted bilayers are converted into H-type FC (H-FC) heterostructure, which has a 2H configuration (Fig. 1d). The SAED patterns of H-FC heterostructure in Fig. 1d indicate that crystalline orientations of WSe_2 and $MoSe_2$ are perfectly aligned after annealing. We also confirmed that R-stack $WSe_2/MoSe_2$ is changed into R-type FC (R-FC) with atomic configuration of 3R after encapsulation annealing (Fig. S3). It was reported that even the hetero-bilayer with zero-twist-angle has the moiré superlattices owing to lattice mismatch between two TMDs[12]. However, we confirmed the absence of both angle and lattice mismatch in the FC heterostructures by analyzing the SAED patterns (Fig. S4). The atomic reconstruction was not observed in the non-encapsulated $WSe_2/MoSe_2$ after annealing under Se-rich environment (Fig. S5). Thus, encapsulation with graphene or hBN is essential for atomic reconstruction because the vertical compression can be induced by encapsulation[22,23]. Furthermore, we also

verify that the similar atomic reconstruction occurs even in randomly stacked multilayers (up to four layers) of WSe_2 and MoS_2 with different twist angles at individual heterointerfaces (Figs. S6-8). Although we separately stacked four monolayers into twisted tetralayers, the whole stack transformed into FC phase after encapsulation annealing. The stacked layers show different critical temperatures for atomic reconstruction, depending on the types and combinations of TMDs. This will be discussed below. We observed no change in hetero-bilayers of $MoS_2/MoSe_2$ and WS_2/WSe_2 with large lattice mismatches of ~4% after annealing up to 1000˚C. This indicates that the atomic reconstruction occurs only in the hetero-bilayer with a small lattice mismatch.

Figure 2 provides an overview of how the atomic reconstruction process of twisted TMD bilayers varies depending on the stacking sequence and the twist angle. The total vdW energy of twisted TMD bilayers calculated in Ref. 26 is plotted as a function of twist angle for R- (red line) and H-stack (blue line) bilayers to show twist-angle-dependent stability of moiré heterostructure and reconstructed phases (Fig. 2a)[26]. If the twist angle of R- and H-stack bilayers is less than critical angle (θ_c), which is almost zero, the stacked bilayers shows spontaneous atomic reconstruction into periodic domains of AB, BA or 2H separated by IC boundaries as illustrated in Fig. 2b and 2c, without any external stimuli to minimize total vdW energy as indicated by dashed arrows in Fig. 2a. The atomic structure of reconstructed domains depends on the stacking sequence, with the R-stack being 3R configuration and H-stack being 2H configuration. Meanwhile, if the twist angle is larger than θ_c, the twisted TMD bilayers maintain incommensurate moiré superlattices because of insufficient thermal energy at room temperature to overcome the energy barrier for spontaneous atomic reconstruction (Fig. 2d). Nevertheless, encapsulation annealing of the twisted TMD bilayers over critical temperature results in atomic reconstruction into the FC structures of Figs. 2e and 2f, regardless of the twist angle and stacking type. The atomic structure of FC bilayers is determined by their stacking type: R(H)-stack transforms into R(H)-FC, which has 3R(2H) atomic configuration.

Structural characteristics of FC heterostructures

HAADF-STEM image of Fig. 3a shows the partially overlapped region of H-stack $WSe_2/MoSe_2$ bilayers with a twist angle of 29.5˚ after encapsulation annealing at 800˚C. The H-FC $WSe_2/MoSe_2$ and its adjacent 1L-$MoSe_2$ area have identical crystal orientation, meanwhile the distant monolayer $MoSe_2$ area retains their original crystal direction as indicated by zigzag directions, resulting in a sharp boundary between two monolayer regions as indicated by blue-dashed line. The difference in crystalline orientations between reconstructed and pristine regions in 1L-$MoSe_2$ is 29.5˚, which corresponds to the twist angle of the as-stacked $WSe_2/MoSe_2$ bilayer. The magnified TEM image of Fig. 3b (red box of Fig. 3a) indicates that the nanometer-wide boundary has a highly distorted lattice structure with a few vacancies, which provides a barrier for propagation of atomic reconstruction. As shown in Fig. 3c, a few hexagonal areas of monolayer WSe_2 with aligned crystalline orientation are observed in the H-FC $WSe_2/MoSe_2$ region. It is estimated that $MoSe_2$ layer with a smaller bond strength or higher defect density forms the nanoscale holes to relax the strain induced by the atomic reconstruction, as reported in an annealed monolayer[27].

To verify the stability of grain boundary during atomic reconstruction, we fabricated $WSe_2/MoSe_2$ bilayers with grain boundaries between H- and R-stack regions using

CVD-grown polycrystalline $MoSe_2$ and single crystal WSe_2 (Fig. S1). We transferred a star-shaped polycrystalline $MoSe_2$, consisting of several grains with opposite crystalline orientations[28-30], onto a single crystal of WSe_2 (Inset of Fig. 3d). After encapsulation annealing, R- and H-FC heterostructures are formed, maintaining a seamless mirror twin boundary (Fig. 3e). This result agrees with that the mirror twin boundary migrates without damage of atomic structure[31]. The nanoscale boundaries of Fig. 3b are present only in monolayer $MoSe_2$ region, while there is no such boundary in the monolayer WSe_2 as shown in Fig. 3d. Our observations indicate that the thermally induced atomic reconstruction in the stacked bilayers occurs *via* rearrangement of atoms in weakly bonded layer, rather than rotation of entire flakes. It agrees well with that $MoSe_2$ has weaker atomic bonding strength than WSe_2 and TMDs with stronger atomic binding energy require higher temperature for atomic reconstruction[32]. However, there is no clear preference whether the bottom or top layer goes through atomic reconstruction in the case of homo-bilayers (Fig. S9).

Momentum-coordinate-matched interlayer excitons in FC heterostructures

In Fig. 4, we investigated excitonic features of H-FC $WSe_2/MoSe_2$ before and after encapsulation annealing by measuring the PL spectra at room temperature. Unlike randomly stacked TMD bilayers[33], the H-FC $WSe_2/MoSe_2$ showed significantly enhanced PL emission of interlayer excitons (X_I) after annealing (Fig. 4a). The momentum mismatch of the first Brillouin zone (BZ) in the twisted TMD layers prohibits radiative recombination of the interlayer excitons by the optical selection rule as shown at the top of Fig. 4b[3]. Meanwhile, the FC bilayers fabricated in this work allow for the radiative recombination of interlayer excitons owing to alignment of the first BZ in momentum space (bottom of Fig. 4b). We also measured PL spectra of randomly stacked $WSe_2/MoSe_2$ by increasing annealing temperature from 400 to 1000˚C (Fig. S10). The PL peak of interlayer excitons emerged after annealing at 800˚C, which is comparable to the temperature at which atomic reconstruction occurs in Figs. 1c-d. Although the shape of WSe_2 and $MoSe_2$ flakes did not change after annealing, PL peaks of interlayer excitons were strongly enhanced (Fig. S11). Uniform PL intensities of interlayer excitons in the H-FC $WSe_2/MoSe_2$ also indicate the homogeneity of atomic reconstruction (Fig. S12). We also used the dark-field TEM (DF-TEM) to verify that whole stacked region has the same orientation after encapsulation annealing (Fig. S13). In case of the R-stack $WSe_2/MoSe_2$, enhanced PL peak of interlayer excitons exhibits a smaller energy due to the interlayer potential induced by intrinsic electric polarization of the 3R structure (Fig. S14-15), which agrees with previous results[34,35]. The PL peaks of intralayer excitons for $MoSe_2$ (X_M) and WSe_2 (X_W) in H-$WSe_2/MoSe_2$ exhibit blue and red shifts after encapsulation annealing, respectively (Fig. 4c). Statistical measurements of PL shifts in Fig. 4d (measured from five samples) clearly shows the opposite shifts of X_M and X_W. Moreover, the Raman spectra of H-$WSe_2/MoSe_2$ show that the A_{1g} peak of $MoSe_2$ blue-shifts, while the A' and E' peaks of WSe_2 red-shift after encapsulation annealing (Fig. S16). This indicates that the compressive and tensile strains are applied to $MoSe_2$ and WSe_2, respectively[36,37]. Therefore, PL shifts of (X_M) and WSe_2 (X_W) in the FC sample correspond to the opposite strains applied to constituent layers generated by formation of the FC heterostructure.

To precisely probe the energy states of interlayer excitons, we measured low-temperature PL spectra of two H-$WSe_2/MoSe_2$ samples with different twist angles of

58.7˚ and 45.5˚ at 77 K before and after encapsulation annealing. The as-stacked samples show different PL features depending on their twist angles: small PL peaks of spin-singlet interlayer excitons (IX_S) and spin-triplet interlayer excitons (IX_T) for 58.7˚ and broad moiré excitons (IX_M) for 45.5˚, which has been reported elsewhere[4,6,7,16,38-40]. In contrast, two H-FC samples fabricated by encapsulation annealing show almost identical PL features with strongly enhanced PL intensities despite the different twist angles: two distinct peaks of IX_S and IX_T due to large splitting of CBM in $MoSe_2$ by strong spin-orbit coupling. The measured PL peak position differences between IX_S and IX_T (24.3-24.6 meV) in Fig. 5a is comparable to the energy difference between up- and down-spin states of $MoSe_2$ (Δ_{CB})[40,41]. In the twisted hetero-bilayers of TMD, the valence band maximum (VBM) of WSe_2 and the conduction band minimum (CBM) of $MoSe_2$ are displaced in the momentum space. The long-range symmetry of moiré superlattices generates a periodic potential that leads to band renormalization by interlayer hybridization of the wavefunctions of two TMDs as depicted in Fig. 5b[7-9,12,36]. Therefore, IX_M (interlayer excitons trapped in the moiré potential) has shown twist-angle-dependent PL characteristics in the twisted hetero-bilayers[3]. However, all H-FC hetero-bilayers fabricated in this work have the identical electronic band structure: the VBM of WSe_2 and CBM of $MoSe_2$ are aligned at the *K* valley in momentum space as shown in Fig. 5c, leading to similar PL characteristics of distinct IX_S and IX_T. Due to the absence of mirror symmetry in out-of-plane direction of hetero-bilayers, IX_T can contribute to radiative recombination in the hetero-bilayers, unlike in monolayer TMDs where IX_T are optically dark[41,42]. As indicated by a blue box in Fig. 5d, the twisted hetero-bilayers show broad PL peaks of interlayer excitons owing to inhomogeneous moiré potential-trap and random distribution of incommensurate domains in near-zero-stacked $WSe_2/MoSe_2$[43-45]. After encapsulation annealing, we achieved much smaller full width half maximum (FWHM) of IX_S and IX_T (~7.84 meV, indicated by a red box) in the H-FC hetero-bilayers than the values in other reports[7,16,41,42,46-51], reaching a thermal limit (kT, ~6.64 meV at 77 K) (Fig. 5d and Fig. S17). The small FWHM value of IX_S and IX_T PL peaks at low temperature also supports the structural homogeneity of the FC structures (Fig. S18).

Therefore, the strong and narrow PL peaks of interlayer excitons close to the theoretical value indicates the formation of uniform FC heterostructures with exactly zero-twist angle.

Conclusion

In this study, we demonstrate a novel approach for achieving FC structures with zero-twist-angle and zero-lattice mismatch by encapsulation annealing of randomly stacked TMD layers. Our method allowed for the selective formation of R- and H-type FC structures can be easily obtained without epitaxial growth. Due to their commensurate structure with aligned momentum-coordinates, the FC heterostructures show strong PL enhancement of the interlayer excitons. These results not only provide a way to fabricate zero-twisted 2D bilayers with R and H-type configurations, but also offer a promising platform for investigating the unexplored properties of such vdW heterostructures, such as interlayer excitons, interlayer valley, and interlayer ferroelectrics. In particular, the R-FC is expected to be useful in research related to a ferroelectricity or photovoltaic properties induced from an intrinsic electrical polarization in the 3R-TMD homo-bilayers[29,52-55].

References

1. Cao, Y. *et al.* Unconventional superconductivity in magic-angle graphene superlattices. *Nature* **556**, 43-50 (2018).
2. Cao, Y. *et al.* Correlated insulator behaviour at half-filling in magic-angle graphene superlattices. *Nature* **556**, 80-84 (2018).
3. Rivera, P. *et al.* Interlayer valley excitons in heterobilayers of transition metal dichalcogenides. *Nat. Nanotechnol.* **13**, 1004-1015 (2018).
4. Yu, H., Liu, G.-B. & Yao, W. Brightened spin-triplet interlayer excitons and optical selection rules in van der Waals heterobilayers. *2D Mater.* **5**, 035021 (2018).
5. Bai, Y. *et al.* Excitons in strain-induced one-dimensional moire potentials at transition metal dichalcogenide heterojunctions. *Nat. Mater.* **19**, 1068-1073 (2020).
6. Shimazaki, Y. *et al.* Strongly correlated electrons and hybrid excitons in a moire heterostructure. *Nature* **580**, 472-477 (2020).
7. Tran, K. *et al.* Evidence for moire excitons in van der Waals heterostructures. *Nature* **567**, 71-75 (2019).
8. Jin, C. *et al.* Observation of moire excitons in WSe_2/WS_2 heterostructure superlattices. *Nature* **567**, 76-80 (2019).
9. Seyler, K. L. *et al.* Signatures of moire-trapped valley excitons in $MoSe_2/WSe_2$ heterobilayers. *Nature* **567**, 66-70 (2019).
10. Carr, S. *et al.* Twistronics: Manipulating the electronic properties of two-dimensional layered structures through their twist angle. *Phys. Rev. B* **95**, 075420 (2017).
11. Liao, M. *et al.* Precise control of the interlayer twist angle in large scale MoS_2 homostructures. *Nat. Commun.* **11**, 2153 (2020).
12. Yuan, L. *et al.* Twist-angle-dependent interlayer exciton diffusion in WS_2-WSe_2 heterobilayers. *Nat. Mater.* **19**, 617-623 (2020).
13. Liao, M. *et al.* Twist angle-dependent conductivities across MoS_2/graphene heterojunctions. *Nat. Commun.* **9**, 4068 (2018).
14. Yoo, H. *et al.* Atomic and electronic reconstruction at the van der Waals interface in twisted bilayer graphene. *Nat. Mater.* **18**, 448-453 (2019).
15. Weston, A. *et al.* Atomic reconstruction in twisted bilayers of transition metal dichalcogenides. *Nat. Nanotechnol.* **15**, 592-597 (2020).
16. Zhao, S. *et al.* Excitons in mesoscopically reconstructed moiré heterostructures. Preprint at https://arxiv.org/abs/2202.11139 (2022).
17. Kenji Yasuda, Xirui Wang, Kenji Watanabe, Takashi Taniguchi & Jarillo-Herrero, P. Stacking-engineered ferroelectricity in bilayer boron nitride. *Science* **372**, 1458-1462 (2021).
18. Holler, J. *et al.* Low-frequency Raman scattering in WSe_2 − $MoSe_2$ heterobilayers: Evidence for atomic reconstruction. *Appl. Phys. Lett.* **117**, 013104 (2020).
19. Rosenberger, M. R. *et al.* Twist Angle-Dependent Atomic Reconstruction and Moire Patterns in Transition Metal Dichalcogenide Heterostructures. *ACS Nano* **14**, 4550-4558 (2020).
20. Quan, J. *et al.* Phonon renormalization in reconstructed MoS_2 moire superlattices. *Nat. Mater.* **20**, 1100-1105 (2021).
21. Zhu, S. & Johnson, H. T. Moire-templated strain patterning in transition-metal dichalcogenides and application in twisted bilayer MoS_2. *Nanoscale* **10**, 20689-20701 (2018).

22. Vasu, K. S. et al. Van der Waals pressure and its effect on trapped interlayer molecules. *Nat. Commun.* **7**:12168 (2016).
23. Han, X. et al. Effects of Hexagonal Boron Nitride Encapsulation on the Electronic Structure of Few-Layer MoS_2. *J. Phys. Chem. C* **123**, 14797-14802 (2019).
24. Ryu, H. *et al.* Anomalous Dimensionality-Driven Phase Transition of $MoTe_2$ in Van der Waals Heterostructure. *Adv. Funct. Mater.* **31**, 2107376 (2021).
25. Li, J., Jia, L., Zheng, X., Peng, C. & Fu, X. Structural and elastic properties of WSe_2: first-principles calculations. *J. Phys.: Conf. Ser.* **1634**, 012145 (2020).
26. Zhu, S., Pochet, P. & Johnson, H. T. Controlling Rotation of Two-Dimensional Material Flakes. *ACS Nano* **13**, 6925-6931 (2019).
27. Chen, J. *et al.* In situ high temperature atomic level dynamics of large inversion domain formations in monolayer MoS_2. *Nanoscale* **11**, 1901-1913 (2019).
28. Liu, Z. *et al.* Strain and structure heterogeneity in MoS_2 atomic layers grown by chemical vapour deposition. *Nat. Commun.* **5**, 5246 (2014).
29. Zheng, W. *et al.* Controlled growth of six-point stars MoS_2 by chemical vapor deposition and its shape evolution mechanism. *Nanotechnology* **28**, 395601 (2017).
30. van der Zande, A. M. *et al.* Grains and grain boundaries in highly crystalline monolayer molybdenum disulphide. *Nat. Mater.* **12**, 554-561 (2013).
31. Zhao, X. *et al.* Healing of Planar Defects in 2D Materials via Grain Boundary Sliding. *Adv. Mater.* **31**, e1900237 (2019).
32. Singh, Y., Back, S. & Jung, Y. Activating Transition Metal Dichalcogenides by Substitutional Nitrogen-Doping for Potential ORR Electrocatalysts. *Chem. Electro. Chem.* **5**, 4029-4035 (2018).
33. Nayak, P. K. *et al.* Probing Evolution of Twist-Angle-Dependent Interlayer Excitons in $MoSe_2/WSe_2$ van der Waals Heterostructures. *ACS Nano* **11**, 4041-4050 (2017).
34. Paradisanos, I. *et al.* Controlling interlayer excitons in MoS_2 layers grown by chemical vapor deposition. *Nat. Commun.* **11**, 2391 (2020).
35. Yang, D. *et al.* Spontaneous-polarization-induced photovoltaic effect in rhombohedrally stacked MoS_2. *Nat. Photonics* **16**, 469-474 (2022).
36. Dadgar, A. M. *et al.* Strain Engineering and Raman Spectroscopy of Monolayer Transition Metal Dichalcogenides. *Chem. Mater.* **30**, 5148-5155 (2018).
37. Horzum, S. *et al.* Phonon softening and direct to indirect band gap crossover in strained single-layer $MoSe_2$. *Phys. Rev. B* **87**, 125415 (2013).
38. Tang, Y. *et al.* Tuning layer-hybridized moire excitons by the quantum-confined Stark effect. *Nat. Nanotechnol.* **16**, 52-57 (2021).
39. Wang, L. *et al.* Correlated electronic phases in twisted bilayer transition metal dichalcogenides. *Nat. Mater.* **19**, 861-866 (2020).
40. Zhang, L. *et al.* Highly valley-polarized singlet and triplet interlayer excitons in van der Waals heterostructure. *Phys. Rev. B* **100**, 041402 (2019).
41. Wang, T. *et al.* Giant Valley-Zeeman Splitting from Spin-Singlet and Spin-Triplet Interlayer Excitons in $WSe_2/MoSe_2$ Heterostructure. *Nano Lett.* **20**, 694-700 (2020).
42. Li, Z. *et al.* Interlayer Exciton Transport in $MoSe_2/WSe_2$ Heterostructures. *ACS Nano* **15**, 1539-1547 (2021).
43. Schubert, E. F., Göbel, E. O., Horikoshi, Y., Ploog, K. & Queisser, H. J. Alloy broadening in photoluminescence spectra of$Al_xGa_{1-x}As$. *Phys. Rev. B* **30**, 813-

820 (1984).
44. Cadiz, F. *et al.* Excitonic Linewidth Approaching the Homogeneous Limit in MoS_2-Based van der Waals Heterostructures. *Phys. Rev. X* **7**, 021016 (2017).
45. Merritt, T. R. *et al.* Photoluminescence lineshape and dynamics of localized excitonic transitions in InAsP epitaxial layers. *Journal of Applied Physics* **115**, 193503 (2014).
46. Hsu, W. T. *et al.* Negative circular polarization emissions from $WSe_2/MoSe_2$ commensurate heterobilayers. *Nat. Commun.* **9**, 1356 (2018).
47. Rivera, P. *et al.* Observation of long-lived interlayer excitons in monolayer $MoSe_2$-WSe_2 heterostructures. *Nat Commun.* **6**, 6242 (2015).
48. Hanbicki, A. T. *et al.* Double Indirect Interlayer Exciton in a $MoSe_2/WSe_2$ van der Waals Heterostructure. *ACS Nano* **12**, 4719-4726 (2018).
49. Alexeev, E. M. *et al.* Emergence of Highly Linearly Polarized Interlayer Exciton Emission in $MoSe_2/WSe_2$ Heterobilayers with Transfer-Induced Layer Corrugation. *ACS Nano* **14**, 11110-11119 (2020).
50. Wu, B. *et al.* Observation of double indirect interlayer exciton in $MoSe_2/WSe_2$ heterostructure. *Nano Research* **15**, 2661-2666 (2021).
51. Mahdikhanysarvejahany, F. *et al.* Temperature dependent moiré trapping of interlayer excitons in $MoSe_2$-WSe_2 heterostructures. *npj 2D Mater. and Appl.* **5** (2021).
52. Ciarrocchi, A. *et al.* Polarization switching and electrical control of interlayer excitons in two-dimensional van der Waals heterostructures. *Nat. Photonics* **13**, 131-136 (2019).
53. Wang, X. *et al.* Interfacial ferroelectricity in rhombohedral-stacked bilayer transition metal dichalcogenides. *Nat. Nanotechnol.* **17**, 367-371 (2022).
54. Deb, S. *et al.* Cumulative polarization in conductive interfacial ferroelectrics. *Nature* **612**, 465-469 (2022).
55. Lukas Rogée, L. W., Yi Zhang, Songhua Cai, Peng Wang, Manish Chhowalla, Wei Ji, Shu Ping Lau. Ferroelectricity in untwisted heterobilayers oftransition metal dichalcogenides. *Science* **376**, 973-978 (2022).
56. Pizzocchero, F. *et al.* The hot pick-up technique for batch assembly of van der Waals heterostructures. *Nat. Commun.* **7**, 11894 (2016).
57. Rokni, H. & Lu, W. Direct measurements of interfacial adhesion in 2D materials and van der Waals heterostructures in ambient air. *Nat. Commun.* **11**, 5607 (2020).
58. Son, J. *et al.* Atomically precise graphene etch stops for three dimensional integrated systems from two dimensional material heterostructures. *Nat. Commun.* **9**, 3988 (2018).

Methods

Chemical vapor deposition growth.

Monolayer crystals of WSe_2 and $MoSe_2$ were synthesized on SiO_2/Si substrates with SiO_2 thickness of 285 nm by chemical vapor deposition (CVD) with 2-inch quartz tube under ambient pressure. To synthesize monolayer WSe_2, a quartz boat with $WO_{2.9}$ powder (99.99%, Alfa Aesar) KI powder (99.99%, Alfa Aesar) was located at the center of the furnace and the SiO_2/Si substrate suspended face-down on top of the boat. Another quartz boat with selenium powder (99.99%, Sigma Aldrich) was located at the upstream of the quartz tube at a distance of 19.5 cm from the center of the furnace. The furnace temperature is raised up to 800˚C at a rate of 50˚C/min and maintained

for 15 min and the furnace was naturally cooled to room temperature. 300 sccm of Ar were flowed for the whole growth process and 10 sccm of H_2 were flowed until start to the cooling process. To synthesize monolayer $MoSe_2$, a quartz boat with MoO_3 powder (99.97%, Sigma Aldrich) was located at the center of the furnace and the SiO_2/Si substrate suspended face-down on top of the boat. Another quartz boat with selenium powder (99.99%, Sigma Aldrich) was located at the upstream of the quartz tube at a distance of 19.5 cm from the center of the furnace. The furnace temperature is raised up to 750˚C at a rate of 50˚C/min and maintained for 20 min and the furnace was naturally cooled to room temperature. 300 sccm of Ar were flowed for the whole growth process, and 10 sccm of H_2 were introduced from 20 minutes to 35 minutes after starting the growth process.

Sample preparation.

Flakes of hexagonal boron nitride (hBN), graphene were first mechanically exfoliated from bulk crystals onto silicon substrates with 285 nm silicon oxide layer. Monolayer WSe_2 and $MoSe_2$ were either mechanically exfoliated from bulk crystals (from HQ Graphene) or synthesized from CVD. The thickness of monolayer WSe_2 and $MoSe_2$ were identified by optical contrast, photoluminescence (PL) measurements, and atomic force microscopy. Next, hBN/WSe_2/$MoSe_2$/hBN heterostructures for PL measurements were assembled with polycarbonate(PC)/polydimethylsiloxane(PDMS) by dry-transfer method[56], and the pick-up temperatures for hBN and TMDs was around 115 ˚C and 75 ˚C. After stacking, heterostructures were transferred onto a clean SiO_2/Si substrate by releasing the PC film from the PDMS lens at a temperature above 180 ˚C. Finally, transferred samples were placed in chloroform for 3 h to remove the PC film covering heterostructures. In similar to hBN-encapsulated TMD bilayers, graphene-encapsulated TMD bilayers for TEM and STEM imaging were fabricated by dry-transfer method. To prevent the degradation of heterostructures during annealing, bi- or tri-layer graphene were used[24]. However, since it is difficult to detach the graphene from the SiO_2/Si substrate due to stronger adhesion force between Gr/SiO_x rather than hBN/SiO_x[57], hBN used as top layer to easily detach the graphene. Thus, hBN/Gr/TMDs/Gr heterostructures were fabricated at first. Next, a XeF_2 gas, which can selectively etch only the hBN remaining the graphene[58], was treated on the heterostuctures to remove the top hBN. To induce the atomic reconstruction in the twisted TMD layers, encapsulated TMD layers were annealed over 800˚C for 3 h in a vacuum of 10^{-4} Torr. Annealing temperature is varied with combination of constituent TMDs: 800˚C for WSe_2/$MoSe_2$ and $MoSe_2$/$MoSe_2$, 900˚C for MoS_2/MoS_2, 950˚C for WSe_2/WSe_2. The raising time of furnace temperature was 1 h and the furnace was naturally cooled to room temperature.

Transmission electron microscopy

TEM samples were prepared by using a poly (methyl methacrylate) (PMMA)-based wet transfer method. Samples on PMMA film were transferred on Si_3N_4 TEM grids (TEM windows, SN100-A20MP2Q05). The PMMA film was removed by placing samples in acetone for 24 h. HAADF-STEM images and SAED patterns were acquired Cs-corrected-monochromated TEM/STEM (Themis Z) at an operating voltage of 80 kV with a probe current of 30 pA, a 25 mrad convergence angle, and a collection angle range of 84-200 mrad.

Raman and PL spectroscopy

Low-frequency Raman spectra were acquired using Raman spectroscopy (Horiba LabRAM HR Evolution) with a 532 nm laser and a spot size of ~ 1 μm. PL spectra were acquired using Raman spectroscopy (JASCO) with a 532 nm laser and a spot size of ~ 1 μm. Micro-PL measurements at low temperature were conducted with a diode-pumped solid-state (DPSS) laser with the wavelength of 532 nm (2.33 eV) and the power of ~100 μW. We used a 40 × objective lens (N.A. = 0.6) to focus the laser on the samples with a spot of ~1 μm in diameter and to collect the PL signals from the samples. A substrate with exfoliated samples was loaded into an optical cryostat (Oxford MicrostatHe2) and cooled down to 10 K with liquid helium. The PL signals from the samples were dispersed with a Horiba TRIAX 320 spectrometer (300 grooves/mm) and was detected with a CCD using liquid nitrogen for cooling. The Raman and PL spectra were obtained at the same position before and after annealing.

Acknowledgements

This work was supported by the National Research Foundation (NRF) of Korea Grant funded by the Korean Government (2021R1A2C3014316, 2021M3F3A2A01037858, 2017R1A5A1014862 (SRC program: vdWMRC center) and the Creative-Pioneering Researchers Program through Seoul National University. S.Y.L. and H.C. acknowledge support by the NRF of Korea Grant funded by the Korean Government (2019R1A2C3006189). K.W. and T.T. acknowledge support from Japan Society for the Promotion of Science (JSPS) KAKENHI (Grant Numbers 19H05790, 20H00354 and 21H05233) and A3 Foresight by JSPS. Support for P.Y.H. was provided by the Illinois Materials Research Science and Engineering Center through the National Science Foundation MRSEC program, award DMR-1720633. G.H.L. acknowledges the support from the Research Institute of Advanced Materials (RIAM), Institute of Engineering Research (IER), Institute of Applied Physics (IAP), and Inter-University Semiconductor Research Center (ISRC) at the Seoul National University.

Author contributions

J.-H.B. and G.-H.L. designed and conceived the project. H.G.K., Y. C., and M.K. performed the TEM and HAADF-STEM imaging. S.Y.L., H.J., J.K. and H.C. performed PL measurements at low temperature. H.R. fabricated the samples for PL measurements. S.C.H. and Y.J. synthesized the TMDs by CVD. K.W. and T.T. supplied the BN crystals. J.-H.B. and G.-H.L. analyzed the data and wrote the paper together.

Data and materials availability

All data needed to evaluate the conclusions are presented in the article and the Supplementary Information.

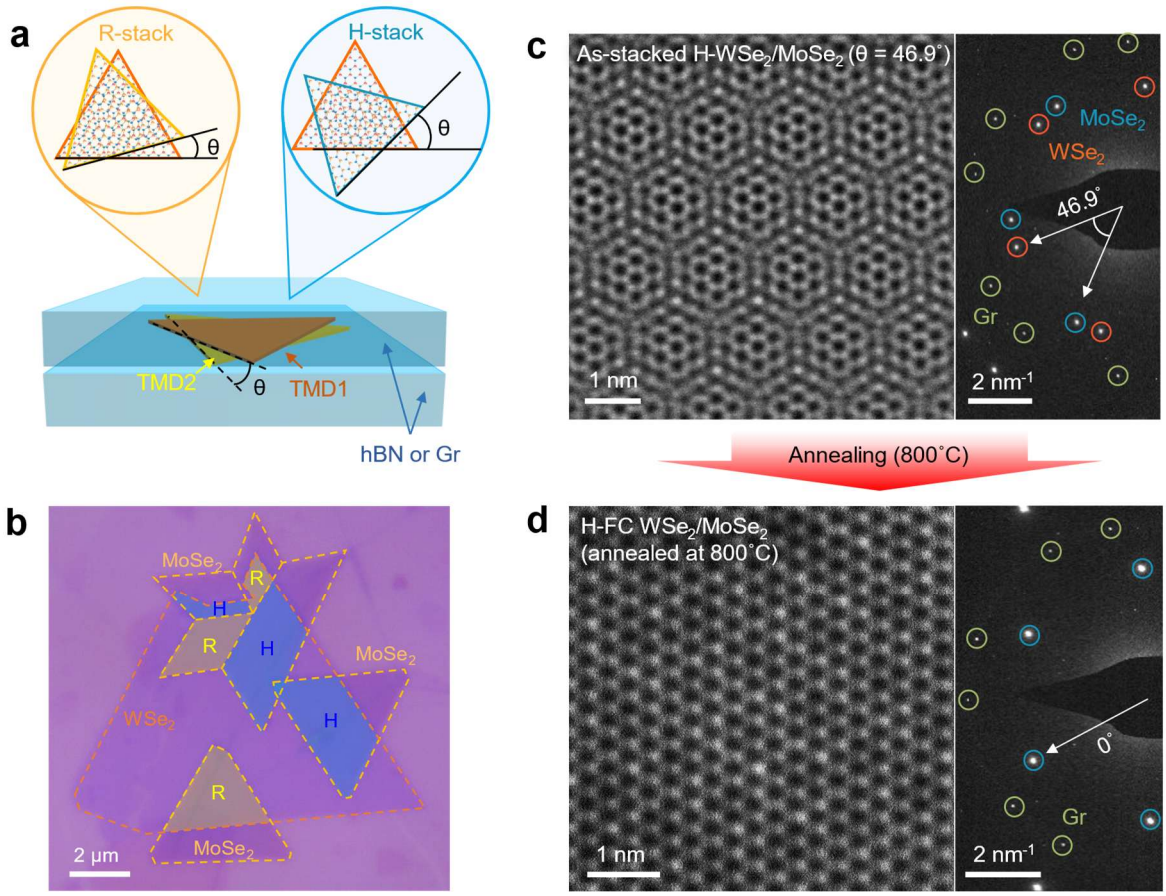

Fig. 1 | Atomic reconstruction to fully commensurate structure in twisted TMD van der Waals heterostructures. a, Schematic images of twisted TMD bilayers encapsulated by graphene or hBN with different stacking type (R- & H-stack). **b**, Optical image of Gr/WSe_2/$MoSe_2$/Gr heterostructures with a different stacking type. False-colored regions indicate R- (yellow) and H-stack (blue) WSe_2/$MoSe_2$ hetero-bilayers. **c**,**d**, High-magnification HAADF-STEM images (left) with SAED images (right) of H-stack WSe_2/$MoSe_2$ HBLs (θ = 46.9˚) as-stacked (**c**) and after annealing (**d**).

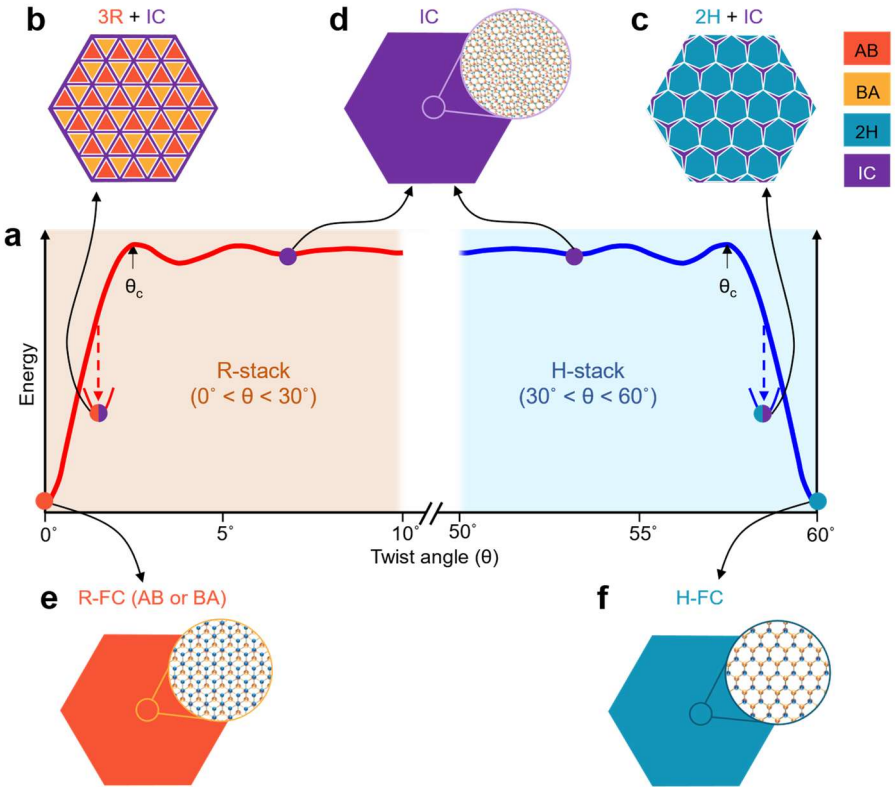

Fig. 2 | Dependence of stacking type and twist angle on the thermally induced atomic reconstruction. a, Schematics of total vdW energy of twisted TMD bilayers as a function of twist angle. **b-f**, Schematic illustrations of atomic structure of twisted TMDs by their stacking type and twist angle before (**b-d**) and after annealing (**e**,**f**). Orange, yellow, blue, and purple domains represent the AB (3R), BA (3R), 2H, and incommensurate (IC) respectively. Red, orange, blue circles represent W, Mo, Se atoms respectively.

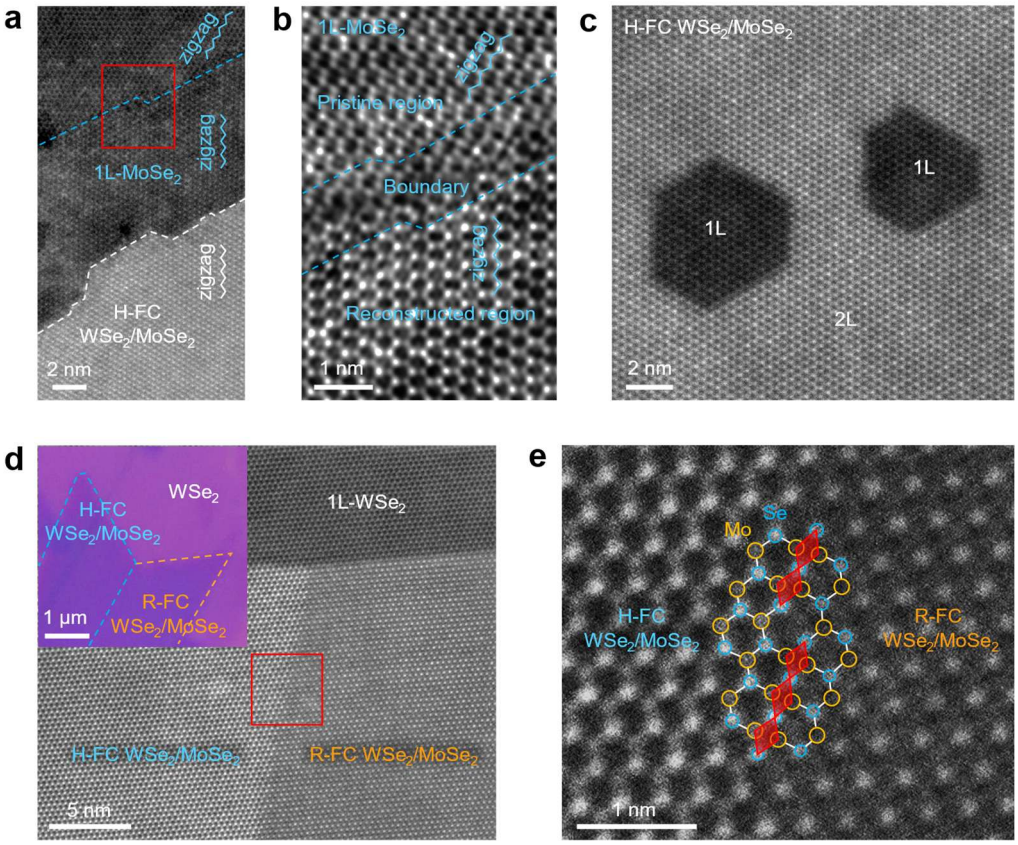

Fig. 3 | Structural characteristics of FC heterostructures. a,**b**, HAADF-STEM images of partially overlapped regions of the $WSe_2/MoSe_2$ (θ = 29.5˚) after annealing. **c**, HAADF-STEM images of hexagonal regions of 1L-TMD in the H-FC $WSe_2/MoSe_2$ after annealing. **d**, HAADF-STEM images of partially overlapped regions single crystal WSe_2 and polycrystalline $MoSe_2$. Inset shows the optical images of twisted $WSe_2/MoSe_2$. **e**, Magnified HAADF-STEM images of the red box in Fig. 3D. Circles represent the Mo (orange) and Se (blue) atoms and red rhombuses represent mirror twin boundaries of $MoSe_2$.

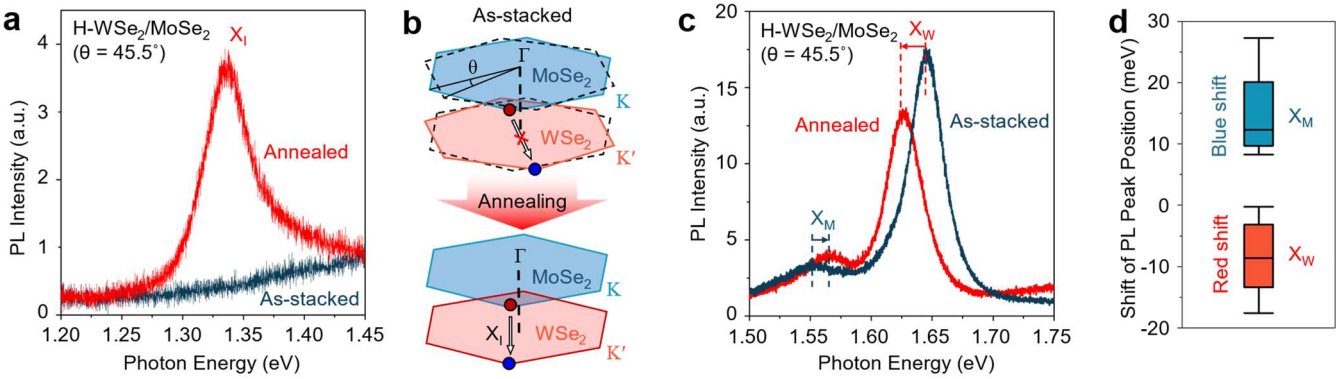

Fig. 4 | PL measurements of hBN-encapsulated H-WSe2/MoSe2 at room temperature. a, Interlayer excitons PL spectra of H-WSe2/MoSe2 (θ = 45.5˚) before and after annealing. **b**, Schematic images of first Brillouin zone of H-WSe2/MoSe2 before and after annealing. Circles represent electrons (red) and holes (blue). **c**, Intralayer excitons PL spectra of H-WSe2/MoSe2 (θ = 45.5˚) before and after annealing. **d**, Shift of PL peak position of intralayer exciton of MoSe2 (X_M) and WSe2 (X_W) *via* encapsulation annealing.

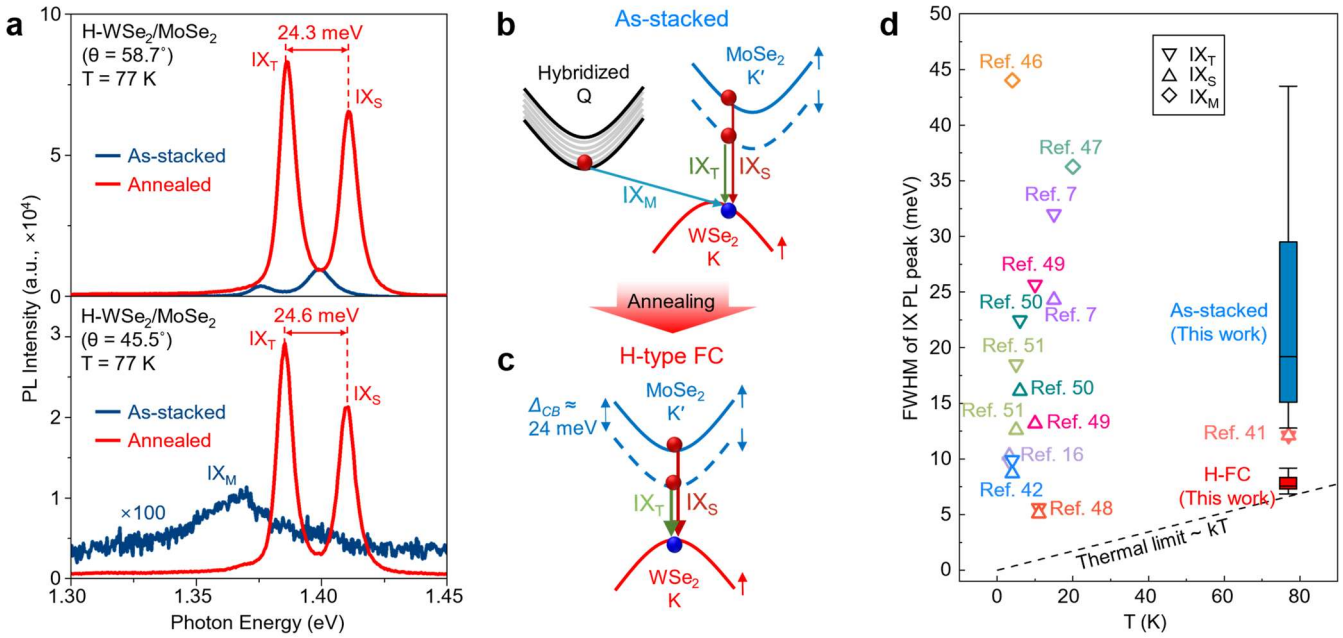

Fig. 5 | PL measurements of hBN-encapsulated H-WSe_2/$MoSe_2$ at 77 K. a, PL spectra of H-stack WSe_2/$MoSe_2$ with $\theta = 58.7^\circ$ and $\theta = 45.5^\circ$ before and after annealing. IX_M is broad IXs PL peaks, and IX_T and IX_S is spin-singlet and –triplet interlayer excitons respectively. **b**,**c**, Schematic images of the band structure of the as-stacked (**b**) and H-type FC (**c**) WSe_2/$MoSe_2$ hetero-bilayers. Circles represent electrons (red) and holes (jade). Solid (dash) lines represent the spin-up (down) bands. **d**, FWHM of PL peaks of interlayer excitons (IX) in H-stack WSe_2/$MoSe_2$.